Applied Physics A (2022) 128:874
https://doi.org/10.1007/s00339-022-06008-8

Applied Physics A
Materials Science & Processing

Multi-phase-field modeling of grain growth in polycrystalline titanium under magnetic field and elastic strain

Y. Rezaei[1] · M. Jafari[2] · A. Hassanpour[3] · M. Jamshidian[4]

Received: 2 July 2022 / Accepted: 26 August 2022

Abstract
A two-dimensional constitutive model was developed to simulate grain boundary motion in polycrystalline titanium exposed simultaneously to magnetic field and elastic strain based on the thermodynamic laws. The multi-scale coupled finite element and multi-phase-field simulations were used to investigate the simultaneous effects of the driving forces arising from the magnetic field and elastic strain energy on microstructure evolution of titanium bicrystalline and polycrystalline samples. The multi-phase-field approach was employed to implement the kinetic relations of grain boundary migration at the mesoscale level. On the other hand, the equilibrium equations were implemented on a macroscale level by the finite element method. Based on the simulation results, the magnetically induced driving force overrides the elastic strain driving force and causes texture evolution toward orientations that contain less magnetic stored energy when the microstructure is exposed to a magnetic field of sufficient strength. Additionally, applying an elastic strain before annealing reduces the time required for magnetic field annealing by accelerating the microstructure evolution. The mean grain size and desired texture grow rapidly when the magnetic field strength and elastic strain are simultaneously increased.

Keywords Multi-phase-field model · Grain growth · Magnetic field · Stressed grain growth

1 Introduction

According to research, the microstructure of a material affects its mechanical behavior [1, 2]. Grain size, grain orientation, and grain boundary (GB) misorientation distribution are decisive parameters in determining the material properties at the macroscale [1, 3–9]. For instance, the performance properties and reliability of thin films in magnetic and electronic components significantly depend on the grain morphology, grain size distribution (GSD), and grain orientations [10]. The control of microstructural evolution is therefore crucial for fabricating materials with optimal magnetic and mechanical properties.

A variety of thermodynamic forces drive microstructural evolution in polycrystalline materials. These driving forces are caused by various factors such as stored deformation energy due to the dislocation structure, GB energy, chemical potential, surface energy, magnetic field, elastic strain energy, and temperature gradient [11–14]. The GB motion can be influenced by elastic strain energy as well as magnetic field driving force originated from a magnetic field by the magnetic susceptibility anisotropy.

Numerous experimental and numerical studies have been conducted regarding the effect of magnetic fields on grain growth [15–25]. The effect of the magnetic field on the GB migration was first reported by Mullins [17]. Molodov et al. [19–21] investigated the effect of magnetic field on grain growth in polycrystalline materials, titanium, and zirconium. The main result of their study was that grain growth kinetics depends on magnetic field direction. Moreover, the grains with energetically preferred orientation grow faster and their volume fraction becomes larger compared with grains with disfavored orientation. He et al. [26] studied the effect of an intense magnetic field on copper. The experimental

✉ M. Jafari
m.jafari@yazd.ac.ir

[1] Mechanical Engineering Group, Pardis College, Isfahan University of Technology, Isfahan 84156-83111, Iran

[2] Department of Mechanical Engineering, Yazd University, Yazd 89158-18411, Iran

[3] Mechanical Engineering Group, Islamic Azad University of Dashtestan, Borazjan 75618-88711, Iran

[4] Department of Mechanical Engineering, Isfahan University of Technology, Isfahan 84156-83111, Iran

Published online: 11 September 2022

results showed that the effect of an external magnetic field is a proper strategy to control polycrystalline microstructural evolution in non-ferromagnetic materials. Rezaei et al. [28] examined the microstructure evolution of titanium polycrystalline subjected to an external magnetic field through the multi-phase-field (MPF) method. A columnar microstructure was used to simulate grain growth in titanium bicrystalline and polycrystalline, and the simulation results were verified with Molodov's experimental results [15, 19]. There have also been several studies on the effect of elastic strain on GB motion [3, 27, 29, 30]. As far as the authors know, no study has been conducted to evaluate the simultaneous influences of magnetic field and elastic strain energy on microstructural evolution by grain growth. Therefore, a constitutive theory is developed based on the MPF approach to examine the simultaneous effect of these driving forces.

Today, the MPF theory is widely employed for modeling and simulating the microstructure evolution. Based on the diffuse GB description, this model is used to explore the microstructure evolution under the influence of several driving forces [31–34]. Kim et al. [35] developed a computational model for MPF simulations of grain growth to apply orientation variables with computationally high potency without restriction. Researchers have used the MPF model to quantitatively and qualitatively predict microstructural evolution under elastic and plastic deformation [36–38]. Roy [39] studied the effect of the interfacial stress on microstructural evolution in NiAl alloys using the phase field approach and showed that interfacial stress affected the stress distribution at interfaces and the phase field solution significantly. In another study, Roy [40] investigated the formation and stability of a nanosized propagating intermediate melt during $\alpha \leftrightarrow \beta$ phase transformation in an HXM nanocrystal. According to this study, the intermediate melt solution can either be continuous reversible or jump-like first-order discontinuous transformation with hysteresis. Jamshidian et al. [4, 11] examined the stressed grain growth using the MPF approach as well as the effect of the representative volume element (RVE) size and microscopic boundary conditions on microstructure evolution.

The aim of this study is to develop a constitutive model based on thermodynamic laws to simulate the grain growth kinetics within a polycrystalline microstructure under the simultaneous impact of a magnetic field and elastic strain. The constitutive model is developed based on our previous works [2, 28] in Sect. 2 to describe the GB migration in polycrystalline RVE under the simultaneous effects of magnetic field and elastic strain on titanium polycrystalline. The thermodynamically consistent framework has been used in our previous works for stressed grain growth, strain-induced grain boundary migration, and magnetic field-induced grain boundary migration separately. The novelty of the present work is using such a description for magnetic field energy and elastic strain energy in a thermodynamically consistent framework to develop the multiphase field constitutive theory, which explains the simultaneous effect of magnetic field and elastic strain energy on the grain growth. In Sect. 3, numerical simulations are performed for the microstructure evolution of titanium bicrystalline and polycrystalline to predict the crystallographic texture and grain size evolution, and the conclusions are given in Sect. 4.

2 Theory

2.1 Constitutive theory on mesoscale

Thamburaja and Jamshidian [2] developed mesoscale constitutive equations based on crystal elasticity and finite deformation to describe grain growth due to elastic deformation in polycrystalline cubic metals. In this section, these mesoscale constitutive equations are further developed to model GB migration under the simultaneous influences of magnetic field and elastic strain. The constitutive theory has been developed through the basic thermodynamics laws and micro-balance theory [41].

The current constitutive framework is developed under constant temperature and without flux/heat sources. In addition, each unique single-crystal orientation is considered a species in which P denotes the number of unique species in the polycrystalline body.

∇, Div, and ∇^2 represent the gradient, divergence, and Laplace operators in the reference configuration, respectively. The governing variables in the constitutive equations are (a) magnetic permeability coefficient (μ_0), (b) magnetic field strength (H), (c) difference in magnetic susceptibility (ΔX), (d) Helmholtz free energy per reference volume (ψ), (e) deformation gradient tensor ($\mathbf{F}$ with $J = \det\mathbf{F} > 0$), (f) absolute temperature ($\theta > 0$) (g), Cauchy stress ($\mathbf{T}$ that $\mathbf{T} = \mathbf{T}^{\mathbf{T}}$) due to angular momentum balance; (h) second Piola–Kirchhoff stress ($\mathbf{T}^* = J\mathbf{F}^{-1}\mathbf{T}\mathbf{F}^{-\mathrm{T}}$), (i) volume fraction (VF) of species i, ξ_i ($0 \le \xi_i \le 1$ with $i = 1, 2, \ldots, P$, and $\sum_{i=1}^{P}\xi_i = 1$). The value $\xi_i = 0$ indicates no species i at that material point on the mesoscale, while $\xi_i = 1$ indicates only species i at that material point. The material point on the mesoscale, which includes two or more species, indicates a point in the GB interface, (j) the micro-stress vector $\mathbf{h}_i$ measured per unit area in the reference body, which operates in response to changes in the VF of species i with $i = 1, 2, \ldots, P$

The MPF variables lists that contain the VF of species and their spatial gradients, are shown with $\xi = (\xi_1, \xi_2, \ldots, \xi_P)$ and $\mathbf{m} = (\mathbf{m}_1, \mathbf{m}_2, ..., \mathbf{m}_p)$, respectively, where $\mathbf{m}_i = \nabla\xi_i$ with $i = 1, 2, \ldots, P$. Using the previous works [33, 35–37], the Helmholtz free energy per unit volume in reference configuration, $\psi = \hat{\psi}(\mathbf{E}, \theta, \mathbf{m}, \xi, H)$ is expressed as follows:

$$\psi = \left(\frac{\sum_{i=1}^{P} g(\xi_i)\psi_i}{\sum_{i=1}^{P} g(\xi_i)} \right) + \psi^m. \tag{1}$$

The first part on the right side of Eq. (1) expresses the composite free energy owing to the existence of several species at the mesoscale material point, where $\psi_i = \hat{\psi}_i(\mathbf{E}_i, \theta, H)$ represents the intrinsic free energy of the species i with the scalar interpolation function $g(\xi_i) = \xi_i^2(3 - 2\xi_i)$. The free energy of microstructure, ψ^m, is given by:

$$\psi^m = \left(\frac{1}{2}\right) \sum_{i=1}^{P} \sum_{s \neq i}^{P} \omega_{is}^{\xi} \xi_i \xi_s - \left(\frac{1}{4}\right) \sum_{i=1}^{P} \sum_{s \neq i}^{P} \epsilon_{is}^{\xi} \mathbf{m}_i . \mathbf{m}_s. \tag{2}$$

Here, the first and second terms indicate the free exchange energy and the gradient-free energy, respectively. ω_{is}^{ξ} and ϵ_{is}^{ξ} are the MPF model parameters [4, 33]. The intrinsic free energy of species i, ψ_i, is expressed as follows:

$$\psi_i = \psi_i^e + \psi_i^\theta + \psi_i^M, \tag{3}$$

where $\psi_i^e = \hat{\psi}_i^e(\mathbf{E}, \theta)$ and $\psi_i^\theta = \hat{\psi}_i^\theta(\theta)$ are, respectively, the thermo-elastic free energy and purely thermal free energy, calculate for species i according to the following equations [41]:

$$\psi_i^e = \left(\frac{1}{2}\right) \{\mathbf{E} - \alpha_i(\theta - \theta_0)\mathbf{I}\} : \mathcal{C}_i[\mathbf{E} - \alpha_i(\theta - \theta_0)\mathbf{I}], \tag{4}$$

$$\psi_i^\theta = c_i[(\theta - \theta_0) - \theta \ln(\theta/\theta_0)]. \tag{5}$$

Here, θ_0 is the reference temperature. $\mathcal{C}_i$, α_i, and c_i are material constants, which indicate symmetric fourth-order elastic modulus tensor, thermal expansion coefficient, and specific heat for the species i, respectively. Due to the cubic symmetry, $\mathcal{C}_i$ is defined by the crystallographic orientation of species i and three elastic constants $\mathcal{C}_{11}$, $\mathcal{C}_{12}$, and $\mathcal{C}_{44}$.

Following the efforts of Molodov et al. [16, 19], the magnetic free energy, $\psi_i^M = \hat{\psi}_i^M(H, \gamma_i)$ is calculated according to the following equation for species i:

$$\psi_i^M = \frac{1}{2}\mu_0 H^2 X_i. \tag{6}$$

where, Ψ_i^M depends on the magnetic field strength (**H**), and the orientation of the magnetic field relative to the principal axis (c-axis) of grain. μ_0 denotes the magnetic permeability coefficient, and $\mathbf{X_i}$ presents the magnetic susceptibility of the grain i, which is determined based on the experimental work as follows [15, 22]:

$$\mathrm{X_i} = \mathrm{X}_\perp + \Delta \mathrm{x} \cos^2 \gamma_\mathrm{i}, \tag{7}$$

where the quantity of $\Delta\mathbf{X}$ is the difference between the values of the magnetic susceptibilities parallel ($\mathbf{X}_\parallel$) and perpendicular ($\boldsymbol{X}_\perp$) to the principal axis of each grain ($\Delta\mathbf{X} = \mathbf{X}_\parallel - \mathbf{X}_\perp$). γ_i is the angle between the principal axis of the grain i, $\boldsymbol{C}_i$, and the magnetic field vector (**H**), which is calculated based on defining dot product as follows [25]:

$$\cos(\gamma_i) = \frac{\mathbf{C_i}.\mathbf{H}}{|\mathbf{C_i}||\mathbf{H}|}. \tag{8}$$

According to Fig. 1, the vectors $\mathbf{C_i}$ and **H** are defined as follows:

$$\mathbf{C} = \left[C \sin(\Phi) \sin\left(\varphi_1\right), -C \sin(\Phi) \cos\left(\varphi_1\right), C \cos(\Phi)\right], \tag{9}$$

$$\mathbf{H} = [H \sin(\alpha) \cos(\beta), H \sin(\alpha) \sin(\beta), H \cos(\alpha)]. \tag{10}$$

As shown in Fig. 1, **H** is demonstrated in terms of the angles α and β, where α indicates the angle between the magnetic field vector and the normal direction (ND), and β denotes the angle between the rolling direction (RD) and the projection of **H** onto RD-TD plane with TD denoting transverse direction. In addition, $\mathbf{C_i}$ is displayed according to Euler angles definition for grain i as $\{\varphi_{1i}, \Phi_i, \varphi_{2i}\}$ [25].

Replacing Eqs. (9) and (10) in Eq. (8) yields:

$$\cos(\gamma_i) = \sin\Phi_i \sin\varphi_{1i} \sin\alpha \cos\beta - \sin\Phi_i \cos\varphi_{1i} \sin\alpha \sin\beta + \cos\Phi_i \cos\alpha. \tag{11}$$

Given the standard thermodynamic arguments and micro-force equilibrium theory [42], the constitutive equations are as follows:

$$\mathbf{T}^* = \frac{\sum_{i=1}^{p} g(\xi_i)\mathcal{C}_i[\mathbf{E} - \alpha_i(\theta - \theta_0)\mathbf{I}]}{\sum_{i=1}^{p} g(\xi_i)}, \tag{12}$$

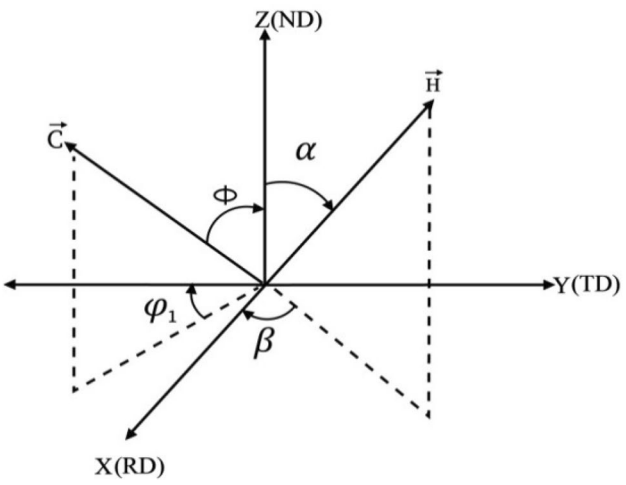

Fig. 1 Magnetic field direction and c-axis with respect to RD, TD, and ND

$$\mathbf{h}_i = \frac{\partial \psi}{\partial \mathbf{m}_i} = -\sum_{s\neq i}^{P} \frac{\epsilon_{is}^{\xi}}{2}\mathbf{m}_s, \quad i,s = 1,2,\ldots,p. \tag{13}$$

Equation (12) is the stress–strain constitutive relationship, and Eq. (13) is the constitutive relationship for micro-stress vectors.

In addition, the kinetic relationship for the MPF variables is given by [2] under the physical constraint $\sum_{i=1}^{P}\xi_i = 1$ and correspondingly $\sum_{i=1}^{P}\dot{\xi}_i = 0$:

$$\frac{\partial \xi_i}{\partial t} = \frac{2}{P^*}\sum_{j\in R} L_{is}\left(f_i - f_s\right) \quad \text{for } i \in R, \tag{14}$$

where, $R = \left\{i, \left|\nabla\xi_i\right| > 0\right\}$ is the set of species at the material point with P^* members interacting with each other. L_{is} is a parameter indicating the MPF mobility for transforming species $i \leftrightarrow s$. The thermodynamic driving force (f_i^{ξ}) for the evolution of species i is given through the following equation:

$$f_i^{\xi} = f_i^m + f_i^e + f_i^{\theta} + f_i^M, \tag{15}$$

where f_i^m shows the curvature driving force:

$$f_i^m = -\sum_{s\neq i}^{P} \frac{\epsilon_{is}^{\xi}}{2}\nabla^2\xi_i - \sum_{s\neq i}^{P}\omega_{is}^{\xi}\xi_s, \tag{16}$$

and f_i^e expresses the elastic strain driving force:

$$f_i^e = \frac{g'\left(\xi_i\right)\left[\sum_{s=1}^{P} g\left(\xi_s\right)\left(\psi_s^e - \psi_i^e\right)\right]}{\left[\sum_{s=1}^{P} g\left(\xi_s\right)\right]^2}, \tag{17}$$

and f_i^{θ} represents the driving force originated from the heterogeneity in the purely thermal free energy:

$$f_i^{\theta} = \frac{g'\left(\xi_i\right)\left[\sum_{s=1}^{P} g\left(\xi_s\right)\left(\psi_s^{\theta} - \psi_i^{\theta}\right)\right]}{\left[\sum_{s=1}^{P} g\left(\xi_s\right)\right]^2}, \tag{18}$$

Finally, f_i^M presents the magnetic-induced driving force:

$$f_i^M = \frac{g'\left(\xi_i\right)\left[\sum_{s=1}^{P} g\left(\xi_s\right)\left(\psi_s^M - \psi_i^M\right)\right]}{\left[\sum_{s=1}^{P} g\left(\xi_s\right)\right]^2}. \tag{19}$$

The MPF model parameters of ω_{is}, κ_{is}, and L_{is} for the species transformation ($i \leftrightarrow s$) are defined based on diffuse GB width (l_{is}^{ξ}), GB energy (σ_{is}^{ξ}), and GB mobility (m_{is}^{ξ}), as follows [12, 33]:

$$\omega_{is}^{\xi} = \frac{4\sigma_{is}^{\xi}}{l_{is}^{\xi}}, \epsilon_{is}^{\xi} = \frac{8}{\pi^2}\sigma_{is}^{\xi}l_{is}^{\xi}, \quad L_{is}^{\xi} = \frac{\pi^2}{8}\frac{m_{is}^{\xi}}{l_{is}^{\xi}}. \tag{20}$$

2.2 Computational homogenization

The developed constitutive equations are applied in multi-scale Taylor computations following the efforts of Jamshidian et al. [1, 2]. For computational homogenization, the macroscale domain is discretized using finite elements, where each finite element integration point represents a macroscopic material point. The macroscopic material point behavior is supposed to be acquired from the homogenized response of the attached RVE. The RVE should have enough grains for a macroscopic material point in the numerical analysis. The MPF approach is employed to implement the kinetic relations of GB migration in the RVE at the mesoscale level. The same RVE is attached to each finite element integration point in the multi-scale model of coupled finite element and MPF. The equilibrium equations are implemented on a macroscale level by the finite element method in Abaqus standard software. It is assumed that the deformation gradient tensor at the mesoscale across the RVE is identical to the macro-deformation gradient tensor, $\overline{\mathrm{F}}$, applied to the macroscale material point. Moreover, it is assumed that the temperature on the mesoscale level across the RVE is equivalent to the macroscale temperature. The RVE is divided into Ω sub-volumes with equal volumes to perform the mesoscale MPF calculations.

The macroscale Cauchy stress $\overline{\mathrm{T}}$ is obtained according to the following Equation at the integration point of finite elements using the Taylor model [2]:

$$\overline{\mathbf{T}} = \frac{1}{\Omega}\sum_{k=1}^{\Omega}\mathbf{T}^k, k = 1,2,\ldots,\Omega, \tag{21}$$

where T^k represents the Cauchy stress tensor in the kth sub-volume within the RVE. The reader is referred to the Appendix for more details on the computational method of the coupled MPF and finite element.

3 MPF simulations

The developed constitutive model is used to simulate the simultaneous influences of magnetic field and elastic strain on microstructure evolution in titanium bicrystalline and polycrystalline samples. The elastic constants for titanium are $\mathcal{C}_{11} = 97.7$ GPa, $\mathcal{C}_{12} = 82.7$ Gpa, and $\mathcal{C}_{44} = 37.5$ GPa at 1000 ℃ according to Ledbetter et al. [43].

3.1 Titanium bicrystalline

Numerical simulations were performed on titanium bicrystalline to achieve a deeper insight into the competition between the magnetic driving force and elastic strain driving force for microstructure evolution. For this purpose, a bicrystalline sample with a flat GB is considered, and the

orientations $(180, 35, \varphi_2)$ and $(0, 35, \varphi_2)$ are selected for the grains as the main orientations for the rolled texture of titanium. Simulations were performed for these orientations with different φ_2 to examine the competitive effect of these driving forces on grain growth. The proposed multi-scale coupled MPF and finite element computational method are used to simulate titanium bicrystalline. A simple cubic geometry is used at the macroscale level with a four-node rectangular element and reduced integration. As shown in Fig. 2, a bicrystalline RVE which includes 200×200 grid points in the directions RD and TD, respectively, with a uniform grid spacing of $Z = 1$ μm is considered. The value of GB width is $l^{\xi} = 6$ μm for all simulations in this section. The RVE is subjected to a simple tensile loading. Therefore, an axial displacement in the TD direction is applied to the samples.

Supposing isotropic GB properties and using Eq. (20), the parameters $L = 0.7511\ \mathrm{m^3 J^{-1} s^{-1}}$, $\omega = 0.2\ \mathrm{MJm^{-3}}$, and $\epsilon = 1.46\ \mathrm{\mu Jm^{-1}}$ are obtained using the GB energy for titanium $\sigma^{\xi} = 0.3\ \mathrm{Jm^{-2}}$ [19]. Finally, the values of the magnetic field parameters are $\mu_0 = 1.26\ \mathrm{\mu NA^{-2}}$ and $\Delta x = 11.8 \times 10^{-6}$.

The elastic stored energy within each grain depends on the angle φ_2, while the magnetic stored energy within each grain depends on the angleφ_2. For this reason, the simulations are performed for different $\varphi_2 = 0, 10, 60^{\circ}$ with $\varphi_1 = 0$, 180 and $\Phi = 35$. As illustrated in Fig. 3, simulations for titanium bicrystalline are accomplished for different strain values of $\varepsilon = 0.002$, 0, and different magnetic field strength values of $H = 0$, 60 $\mathrm{MAm^{-1}}$ for differentφ_2. Regardless of the applied strain $\varepsilon = 0$, the magnetic field causes the GB to move away from the grain with less stored energy with orientation $(180, 35, \varphi_2)$ toward the grain with more stored energy with orientation $(0, 35, \varphi_2)$ as depicted in Fig. 3a. Moreover, it has been shown that the changes of φ_2 have no effect on the GB motion for this state.

The simulation results for the applied strain $\varepsilon = 0.002$ are displayed in Fig. 3b without considering the magnetic field.

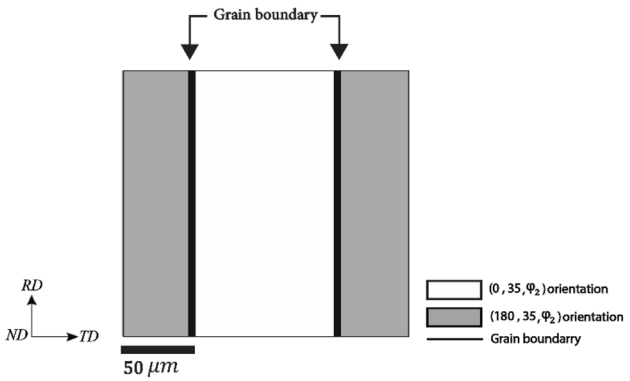

Fig. 2 The RVE of titanium bicrystalline for numerical simulation

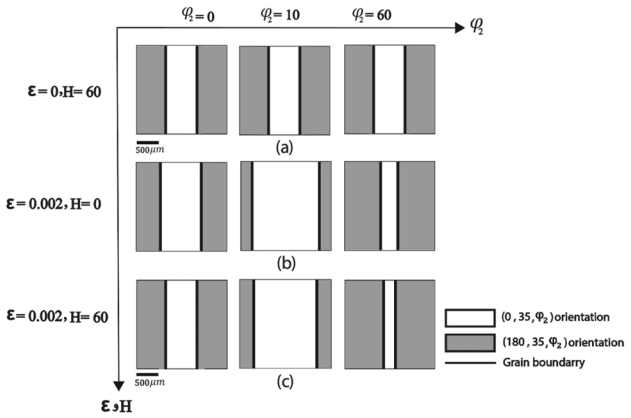

Fig. 3 The simulation results for bicrystalline sample under the simultaneous influences of magnetic field and elastic strain for different φ_2 **a** $\varepsilon = 0$ and $H = 60$ $\mathrm{MAm^{-1}}$, **b** $H = 0$ and $\varepsilon = 0.002$, **c** $H = 60$ $\mathrm{MAm^{-1}}$ and $\varepsilon = 0.002$

As illustrated in Fig. 3b, the GB migration depends on the angle φ_2. When the zero value is considered for φ_2, the elastic stored strain energy is identical for both grains, and the GB has no motion. While the GB moves from the grain with orientation (0, 35, 10) towards the grain with orientation (180, 35, 10) for $\varphi_2 = 10$. For $\varphi_2 = 60$, the GB moves away from the grain with orientation (180, 35, 60) with less stored elastic strain energy toward the grain with orientation (0, 35, 60) with more stored elastic strain energy.

The final state of the simulation is performed by considering magnetic and elastic strain driving forces. The magnetic field with strength $H = 60$ $\mathrm{MAm^{-1}}$ and elastic strain with the value of $\varepsilon = 0.002$ are applied to the RVE. The driving force due to the magnetic field alone causes the GB motion by considering $\varphi_2 = 0$ because the driving force resulting from the elastic strain does not affect the GB migration. This result is like case (a). There is a competition between the two driving forces for $\varphi_2 = 10$. The GB motion amount for the grain (0, 35, 10) is lesser compared to the case (b) because the driving force caused by the magnetic field is trying to move the GB towards the grain (0, 35, 10) in the opposite direction of the elastic strain driving force. Finally, for $\varphi_2 = 60$, both driving forces cause the GB migration away from the grain with orientation (180, 35, 60) towards the grain with orientation (0, 35, 60).

Moreover, the simulations were also performed for $\varphi_2 = 20, 30, 40, 50$. Therefore, the GB motion is like the case with $\varphi_2 = 10$ considering $\varphi_2 = 20, 30, 40$, but occurs at a lower speed. In addition, the boundary migrates like the case with $\varphi_2 = 60$ for $\varphi_2 = 50$, but the GB migration is slower.

3.2 Titanium polycrystalline

This section investigates the microstructure evolution for titanium polycrystalline under the simultaneous effects of a simple tension loading and magnetic field. In a titanium polycrystalline sample, the interaction between elastic strain driving force, magnetic driving force, and curvature driving force is studied. A simple cubic geometry with an integration point in its center is used at macroscale, and a uniaxial tensile loading is applied in the TD direction. The directions ND, TD, and RD relative to the applied magnetic field on the titanium sheet are according to Fig. 4a. As shown in Fig. 4b and c, an RVE is attached to the integration point of the finite element at the macroscale level. This RVE includes 2000×2000 elements in the directions RD and TD, respectively, and a uniform grid with spacing $Z = 1$ µm. The diffuse GB width is six grids spacing ($L = 6$ µm) for all simulations performed in this section. The RVE displayed in Fig. 4c includes 2632 grains with an initial mean grain size of 39 µm. According to Fig. 4c, the initial polycrystalline texture consists of grain sets with orientations $(0, 35, \varphi_2)$ and $(180, 35, \varphi_2)$ with corresponding percentages of 50% and 48%, respectively. The orientations φ_1 of the remaining grains are random. As shown in Fig. 4d, the initial GSD of the RVE is log-normal. This texture is similar to the texture of commercially pure titanium polycrystalline used in the experimental study of Molodov et al. [19]. All the magnetic field and GB parameters are considered according to Sect. 3.1.

The curvature driving force and the mean grain diameter are inversely proportional. Moreover, grain orientation does not affect the curvature driving force [44]. In addition, the elastic strain driving force depends highly on the initial grain orientations and is independent of the mean grain diameter value. The magnetic field driving force strongly depends on the magnetic field strength and orientations of the grains relative to the magnetic field. The simulations are performed for two case studies. The first case study simulations are conducted for constant magnetic field strength and different applied strains, while different magnetic field strengths and constant applied strain are considered for the second case study.

The effect of different applied strains on the microstructure evolution of a titanium polycrystalline is investigated as follows. Simulations are carried out for three different values of applied strain ($\varepsilon = 0.0005,\ 0.001$ and 0.002) at a constant magnetic field with the strength of $H = 13.5$ MAm^{-1}. Different values of strain and magnetic field strength, the GB width and the final times when the simulations are stopped, are given in Table 1.

The simulation ceases at final time t_f when the mean grain diameter is twice the initial mean diameter ($D = 2.8D_0$). The results of MPF simulations for the microstructure evolution, VF and mean grain size for different

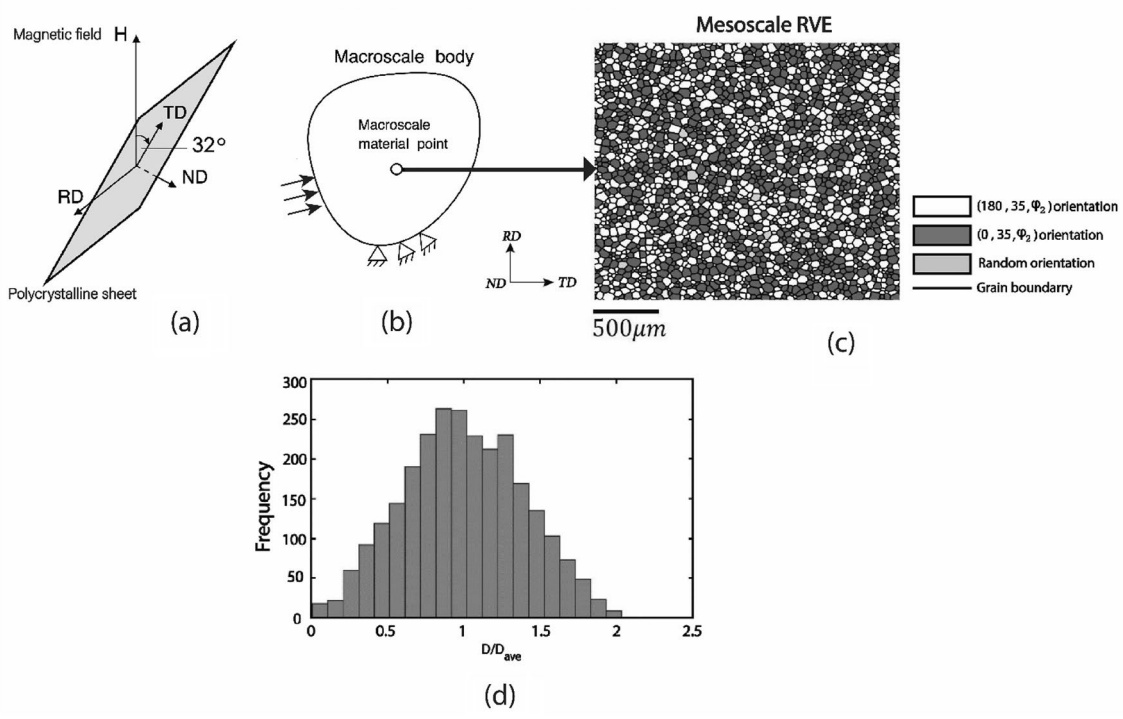

Fig. 4 **a** The schematic of ND, TD and RD directions concerning the applied magnetic field on the titanium sheet, **b** a continuum body at macroscale level under a simple tensile loading, **c** the RVE at the mesoscale level attached to that macroscopic material point, **d** the initial normal GSD

Table 1 Different values of applied strain in simulating microstructure evolution in titanium polycrystalline, magnetic field strength, corresponding values of GB width, MPF parameters, and final times when the simulations are stopped

Case of simulation	D_0 [μm]	z [μm]	l [μm]	ε	H [MAm^{-1}]	t_f [min]
1	39	1	6	0.0005	13.5	91.1
2	39	1	6	0.001	13.5	66.9
3	39	1	6	0.002	13.5	38.1

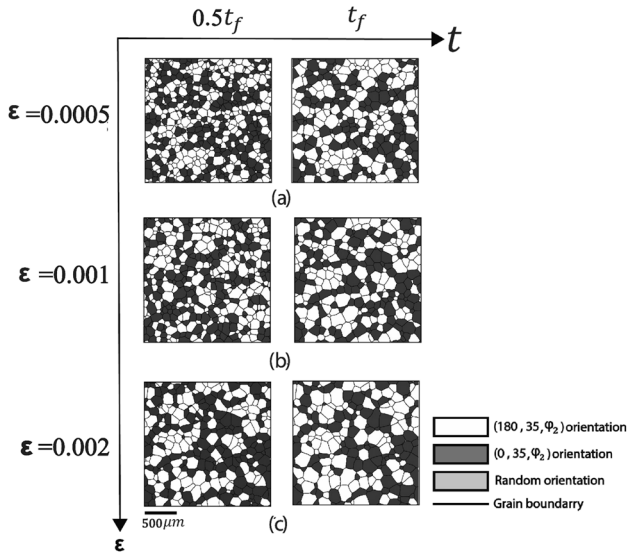

Fig. 5 The simulation results of microstructure evolution of titanium polycrystalline subjected to a magnetic field with a strength of $H = 13.5$ MAm^{-1} with strains **a** $\varepsilon = 0.0005$, **b** $\varepsilon = 0.001$, and **c** $\varepsilon = 0.002$ at $t = 0.5t_f$ and $t = t_f$.

values of applied strain are shown in Figs. 5, 6, 7. Parameters $\overline{D}$, $\overline{D}_1$, $\overline{D}_2$, V_1, and V_2 are the mean diameter of all grains, grain set $(180, 35, \varphi_2)$, grain set $(0, 35, \varphi_2)$, VF of grain set $(180, 35, \varphi_2)$, and VF of grain set $(0, 35, \varphi_2)$, respectively.

The microstructure evolution for different values of strain, i.e., $\varepsilon = 0.0005$, 0.001, and 0.002, and constant magnetic field with a strength of $H = 13.5$ MAm^{-1} are illustrated in Fig. 5 at the times $t = 0.5\ t_f$ and $t = t_f$. The grains with random φ_1 disappear by applying strain, and only grains with orientation $(180, 35, \varphi_2)$ and $(0, 35, \varphi_2)$ remain within the microstructure. The reason is that the grain sets $(0, 35, \varphi_2)$ and $(180, 35, \varphi_2)$ have the minimum stored elastic strain energy, while the grains with random φ_1 possess a higher amount of stored elastic strain energy, which eliminates these grains. It can be observed that the driving forces owing to the magnetic field, elastic strain, and GB curvature do not lead to a significant change in the morphology of the grains in the microstructure.

The mean diameter of grain sets $(0, 35, \varphi_2)$ and $(180, 35, \varphi_2)$ for different values of strain are investigated during grain growth to quantify the microstructure evolution of titanium polycrystalline. As Fig. 6 depicts, the time that the mean grain diameter reaches 2.8 times the initial mean grain diameter is $t = 91.1$, 66.9, and 38.1 min for the applied strains $\varepsilon = 0.0005$, 0.001, and 0.002, respectively. Therefore, the mean grain size grows more rapidly by increasing the applied strain. In other words, as applied strain increases, there will be a greater difference in the stored elastic strain energy across the GB. Moreover, Fig. 6b–d illustrate that the difference in the mean grain size in the $(0, 35, \varphi_2)$ and $(180, 35, \varphi_2)$ grain sets is insignificant for different strains $\varepsilon = 0.0005$, 0.001, and 0.002 because the stored elastic strain energy for grain sets $(0, 35, \varphi_2)$ and $(180, 35, \varphi_2)$ is almost equal.

The VF evolution of grain sets $(0, 35, \varphi_2)$ and $(180, 35, \varphi_2)$ subjected to a magnetic field with strength $H = 13.5$ MAm^{-1} and under different strains $\varepsilon = 0.0005$, 0.001 and 0.002 are depicted in Fig. 7 during the annealing time. The stored elastic strain energy for grain sets $(0, 35, \varphi_2)$ and $(180, 35, \varphi_2)$ depends on the angle φ_2. Since φ_2 is randomly distributed for both grain sets, the stored elastic strain energies for $(0, 35, \varphi_2)$ grains and $(180, 35, \varphi_2)$ grains are almost identical. Therefore, no significant change is observed in the texture, which is also seen in the simulation results for the bicrystalline RVE.

The effect of magnetic field strength is investigated for constant applied strain $\varepsilon = 0.002$ on microstructure evolution in titanium polycrystalline RVE. The simulations are performed for different magnetic field strength values including $H = 13.5$, 30, and 60 MAm^{-1}. Based on the previous simulations, the magnetic field is applied in the same direction. Table 2 shows the different values of magnetic field strength, MPF parameters, and final times when the simulations are stopped. The simulation ceases at the final time (t_f) when the mean grain diameter is twice the initial mean grain diameter ($\overline{D} = 2.6D_0$).

The simulation results for the microstructure evolution, mean grain size, and VF for different magnetic field strength values are shown in Figs. 8, 9, 10, respectively. Figure 8 displays the microstructure evolution for $H = 13.5$, 30, and 60 MAm^{-1} and constant strain $\varepsilon = 0.002$ at the times $t = t_f$ and $t = 0.5\ t_f$. As the magnetic field strength increases, the $(180, 35, \varphi_2)$ grains, that are preferred by the stored magnetic energy, prevail over other grains during the annealing

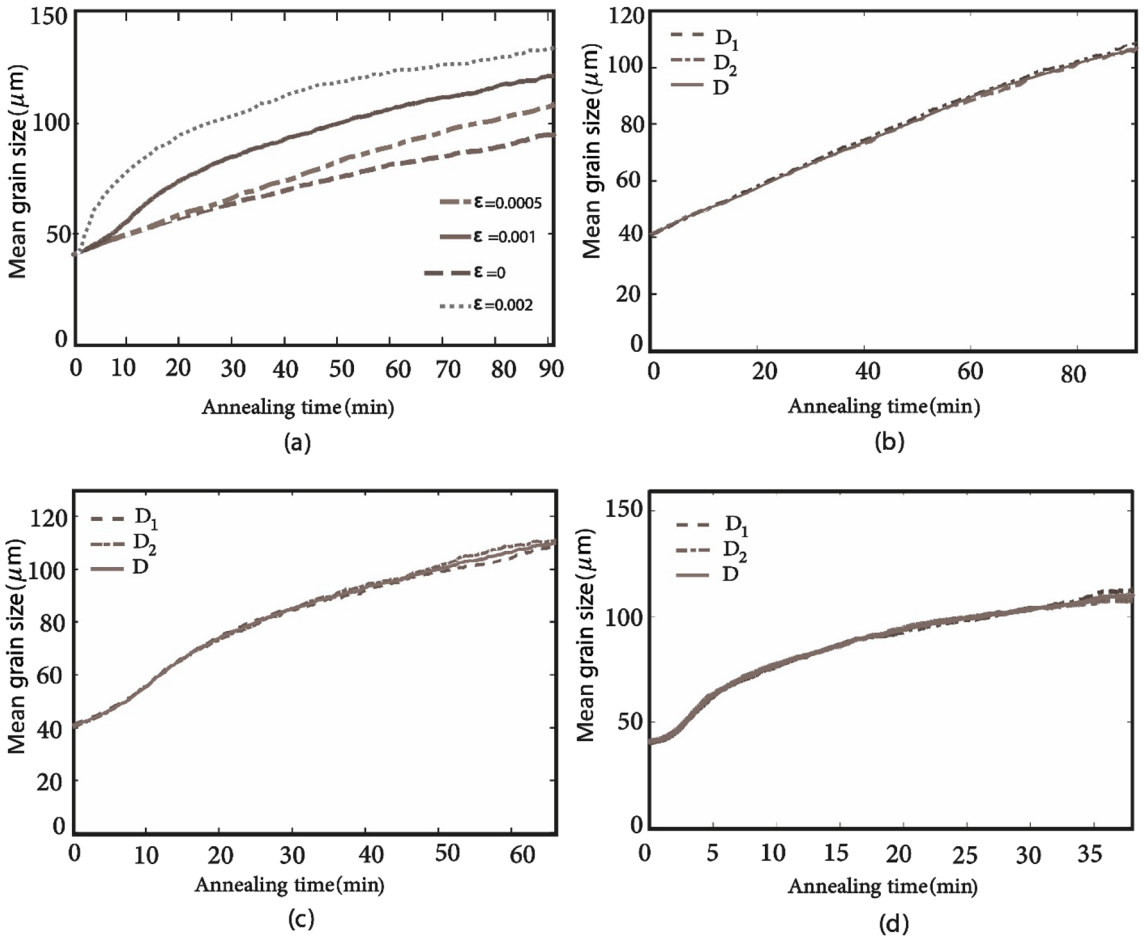

Fig. 6 The evolution of mean grain size **a** for all grains subjected to a constant magnetic field with a strength of $H = 13.5$ MAm^{-1} and different strains, and the evolution of mean grain size for all grains, D, $(0, 35, \varphi_2)$ grains, D_1, and $(180, 35, \varphi_2)$ grains, D_2, subjected to a constant magnetic field with a strength of $H = 13.5$ MAm^{-1} and different strains **b** $\varepsilon = 0.0005$, **c** $\varepsilon = 0.001$, and **d** $\varepsilon = 0.002$ during the annealing time

time. In other words, the magnetic driving force overcomes the elastic strain driving force under the sufficient strength of the magnetic field. Grains with random φ_1 are eliminated due to the presence of elastic strain energy driving force.

Figure 9 demonstrates the mean grain size evolution for grain sets $(0, 35, \varphi_2)$ and $(180, 35, \varphi_2)$ as well as all grains. As shown in this figure, the time when the mean grain diameter reaches 2.6 times the initial mean grain diameter is $t = 36.4$, 35.4, and 32.8 min for the applied magnetic field with strengths of $H = 13.5$, 30, and 60 MAm^{-1}, respectively. This observation indicates that the magnetic field strength has little effect on the grain growth rate. This result is consistent with the experimental results of Molodov et al. [19]. As the magnetic field strength increases, the $(180, 35, \varphi_2)$ grains with less magnetic energy than other grains grow faster than the $(0, 35, \varphi_2)$ grains. In the case where the magnetic field is the highest, this difference is most apparent.

To quantify the evolution of grain VF, the VFs of two grain sets $(0, 35, \varphi_2)$ and $(180, 35, \varphi_2)$ for different magnetic field strength values are examined during microstructure evolution as depicted in Fig. 10. The VF of grain set $(180, 35, \varphi_2)$ increases and VF of grain set $(0, 35, \varphi_2)$ decreases by increasing the magnetic field strength. Hence, the grains of set $(180, 35, \varphi_2)$, which are preferred by possessing less stored magnetic energy than other grains, consume other grains. Therefore, increasing the magnetic field strength can intensify the preferential texture.

The simulation results for the four cases with minimum and maximum magnetic field strength and applied uniaxial strain are shown in Fig. 11 to further investigate the effects of driving forces arising from the magnetic field, elastic strain, and GB curvature on the grain growth in titanium polycrystalline. Figure 11 demonstrates the microstructure evolution subjected to the magnetic field with a strength of $H = 0$, 60 MAm^{-1} and applied strains $\varepsilon = 0$, 0.002. When the zero value is considered for magnetic field strength and

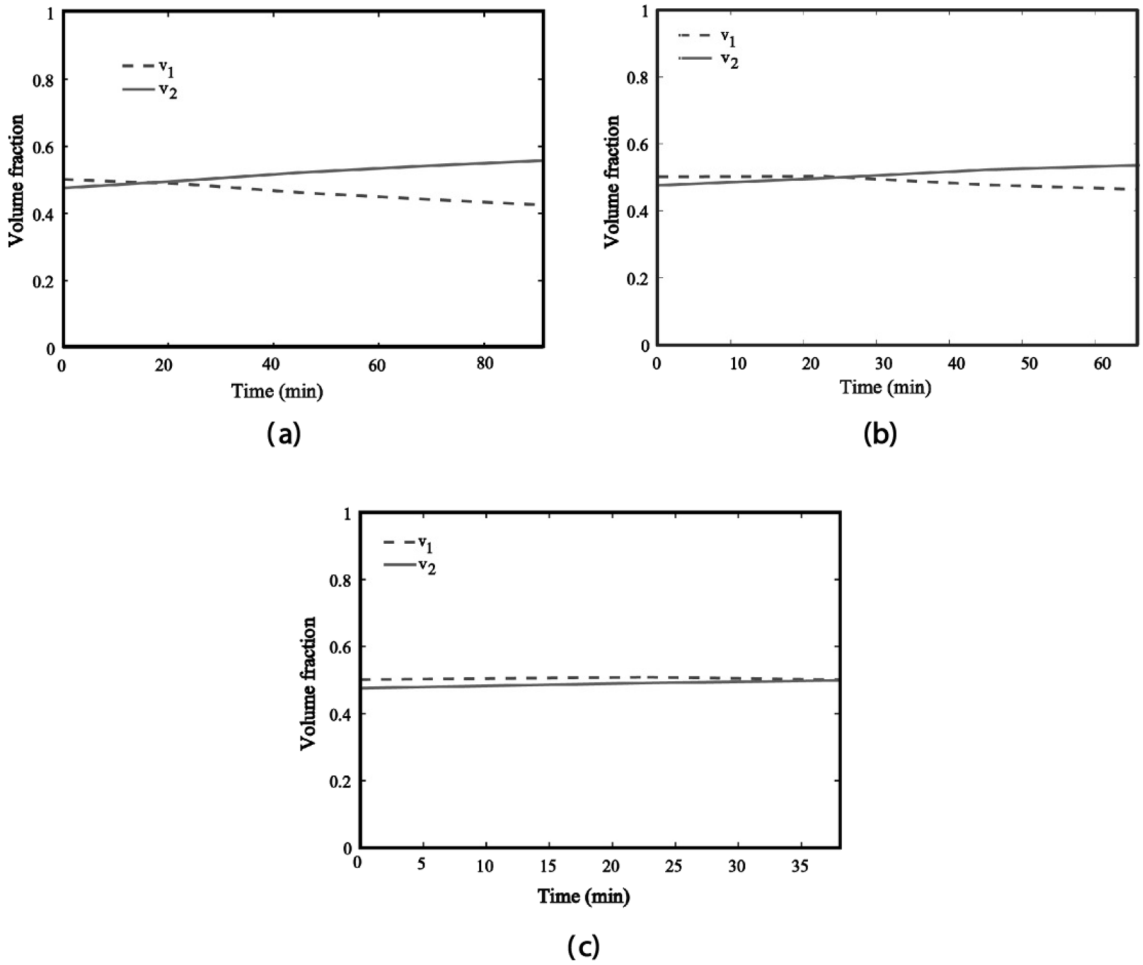

Fig. 7 The VF evolution of grain sets $(0, 35, \varphi_2)$, v_1, and $(180, 35, \varphi_2)$, v_2, subjected to a magnetic field with strength of $H = 13.5$ MAm^{-1} and different strains **a** $\varepsilon = 0.0005$, **b** $\varepsilon = 0.001$, and **c** $\varepsilon = 0.002$, over the annealing time

Table 2 Different strengths of the applied magnetic field in simulating microstructure evolution in titanium polycrystalline, applied strain value, corresponding values of GB width, MPF parameters, and final times when the simulations cease

Case of simulation	D_0 [μm]	z [μm]	l [μm]	ε	H [MAm^{-1}]	t_f [min]
1	39	1	6	0.002	13.5	36.4
2	39	1	6	0.002	30	35.4
3	39	1	6	0.002	60	32.8

strain, the only driving force affecting the GB motion is the curvature driving force, which causes normal growth of grains. Thus, the texture does not change without elastic strain and magnetic field, $H = \varepsilon = 0$. However, the preferential growth of $(180, 35, \varphi_2)$ grains occurs during microstructure evolution by increasing the magnetic field intensity ($H = 60$) and without the applied strain ($\varepsilon = 0$). Moreover, the grains with random φ_1 are not completely consumed.

On the other hand, the main texture in the microstructure does not change during grain growth by increasing the elastic strain and in the absence of a magnetic field. However, the microstructure evolution rate increases. Under sufficient magnetic field and elastic strain, the magnetically induced driving force overcomes the elastic strain driving force as illustrated in Fig. 11d. This leads to the growth of grain set $(180, 35, \varphi_2)$ and the removal of other grains.

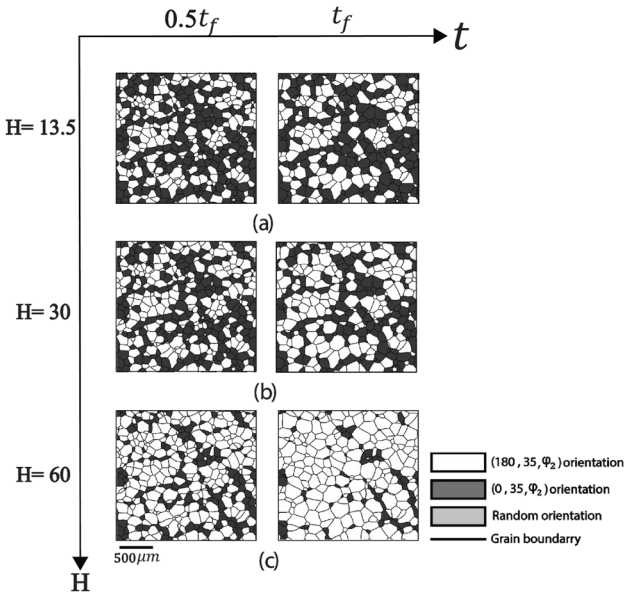

Fig. 8 The simulation results of microstructure evolution for titanium polycrystalline with constant strain $\varepsilon = 0.002$ and different magnetic field strengths of **a** $H = 13.5$ MAm^{-1}, **b** $H = 30$ MAm^{-1}, and **c** $H = 60$ MAm^{-1} at times $t = 0.5t_f$ and $t = t_f$

Figure 12a and b display the mean grain size evolution and VF for the four simulation cases. As these figures show, no change in the VF is observed when the magnetic field and strain are both zero. The VF of $(180, 35, \varphi_2)$ grains grows quickly for the magnetic field strength $H = 60$ without applied strain, whereas the mean grain size evolution experiences a small change compared to the case with $H = 0$ and $\varepsilon = 0$. The mean grain size increases rapidly with the applied strain $\varepsilon = 0.002$ without the magnetic field. In this case, the primary texture persists during microstructure evolution. When both the strain and magnetic field are applied, there is a rapid increase in the mean size of grains as well as the growth of the preferential texture. Therefore, the obtained results express that applying slight strain to the sample before the magnetic field annealing significantly changes the grain growth rate, and the required time for magnetic annealing decreases.

Figure 13 shows the GSD histograms for different magnetic field strengths and applied strains. The GSD histograms remain log-normal as in the initial state by applying a sufficient magnetic field, but the heights of the histogram bars decrease. Therefore, the magnetic driving force accelerates the growth of the desired grains but does not affect the GSD. On the other hand, the heights of the histogram bars decrease significantly by increasing the applied strain, and the graphs deviate from the initial log-normal distribution, indicating that the elastic strain driving force changes the GSD histograms.

4 Conclusion

A 2D constitutive model was presented for simulating GB migration affected by elastic strain and magnetic field based on thermodynamic laws. The developed constitutive equations were implemented in a semi-concurrent multi-scale framework utilizing the Taylor homogenization method. The stress–strain response of the structure was modeled through the finite element method at the macroscale, while the grain growth kinetics in a polycrystalline RVE subjected to strain and magnetic field was performed by MPF simulation.

The simulations were carried out on pure titanium bicrystalline and polycrystalline according to the experimental work of Molodov [19]. The simultaneous effects of applied elastic strain and magnetic field were investigated on the microstructure evolution. Generally, the following results were obtained:

- The elastic strain driving force had an outstanding effect on the grain growth rate, which increased by raising the applied strain at a constant magnetic field.
- The magnetic field driving force had no significant effect on the grain growth rate, which experienced no significant changes by increasing the applied magnetic field at a constant applied strain.
- Applying elastic strain to the microstructure before the magnetic field annealing decreased the required time for the annealing.
- Increasing the magnetic field strength caused the $(180, 35, \varphi_2)$ orientation to become the dominant texture.
- The driving force owing to the elastic strain had a significant effect on the GSD than the driving force originated from the magnetic field.

Appendix: Numerical implementation

A semi-concurrent multi-scale time-integration method was used for the numerical implementation of the constitutive equations using Thamboraja and Jamshidian [2]. This multi-scale coupled MPF and finite element computational method is implemented in Abaqus standard finite element software by writing a UMAT subroutine. The details of the numerical algorithm for the time integration method are as follows:

The index λ represents the integration point of finite elements, where $\lambda = 1, 2, \ldots, \lambda_{el}$ and λ_{el} represent the total number of integration points of the finite elements. The index $k = 1, 2, \ldots, \Omega$ is used to represent the grid points of RVE, where Ω represents the total number of grid points.

The quantity of a variable at the grid points of the RVE is the mesoscale quantity, whereas a quantity at finite element integration points is a macroscale quantity. The quantity #

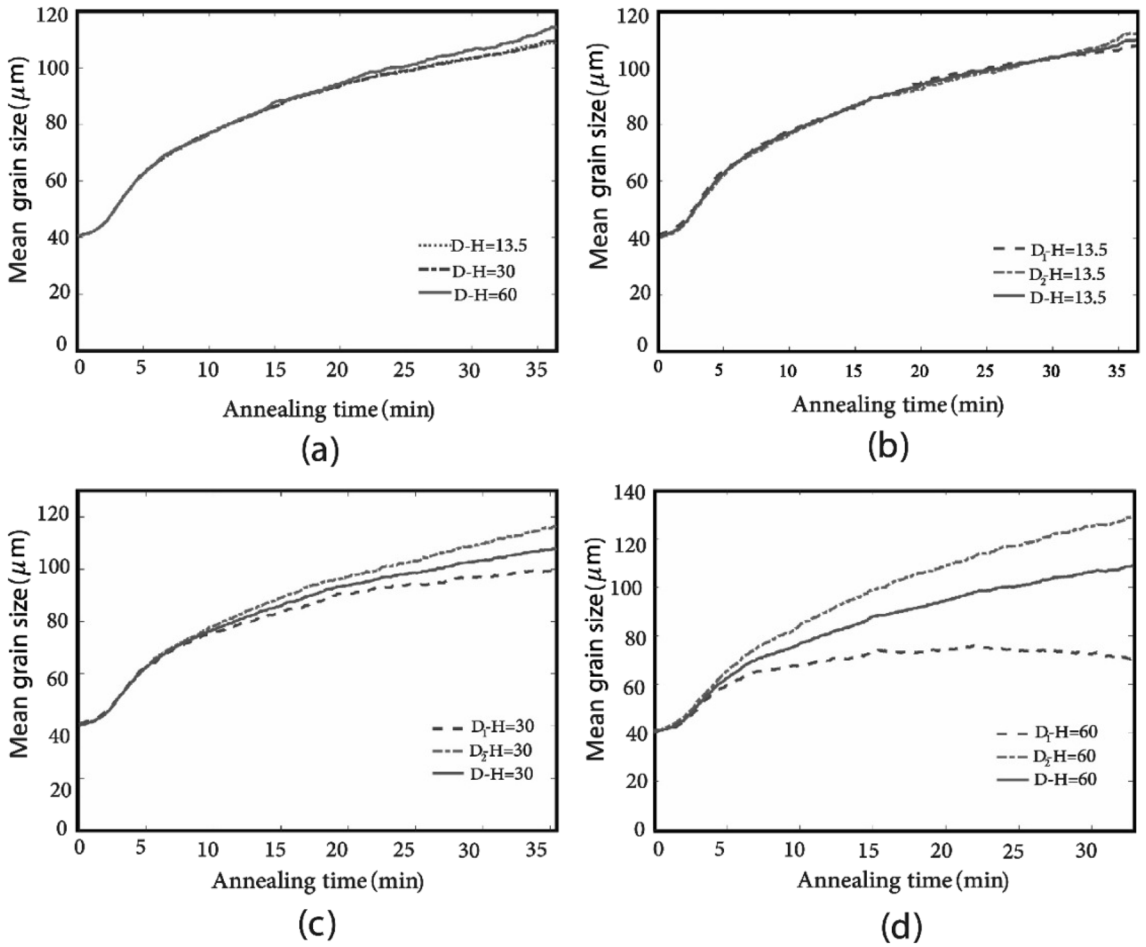

Fig. 9 The mean grain size evolution **a** for all grains with constant strain $\varepsilon = 0.002$ and magnetic field with strengths of $H = 13.5$, 30, and 60 MAm^{-1}, and the evolution of mean grain size for all grains, $(0, 35, \varphi_2)$ grains and $(180, 35, \varphi_2)$ grains for constant strain value $\varepsilon = 0.002$ and magnetic field with strengths of **b** $H = 13.5$ MAm^{-1}, **c** $H = 30$ MAm^{-1}, and **d** $H = 60$ MAm^{-1} over the annealing time

at the integration point of elements λ is represented as $\#^{\lambda}$. The quantity # is displayed as $\#^{\lambda,\kappa}$ in the K-the point of the grid from the RVE attached to the integration point of the λ finite elements.

In the numerical algorithm process, we only track species at a grid point at that grid point and its nearby vicinity [2, 44]. The A_p list represents a set containing species, which satisfy condition $0 < \xi_i \leq 1$ at the grid point and its nearest neighboring points. In addition, each member of the A_p set is unique.

In this paragraph, the discussion is limited to the RVE attached to the integration point of the finite elements λ. The grid point number K in the RVE is labeled as$G^{\lambda,\kappa}$, which is in position (x_1, x_2, x_3) in the reference configuration. Grid points in positions $(x_1 + z, x_2, x_3)$, $(x_1 - z, x_2, x_3)$, $(x_1, x_2 + z, x_3)$, $(x_1, x_2 - z, x_3)$, and $(x_1, x_2, x_3 + z)$, $(x_1, x_2, x_3 - z)$ are known in the reference configuration as the neighboring grid points of $G^{\lambda,\kappa}$ where Z represents the uniform spacing of the grid. The grid point index for each of the neighboring grid points of $G^{\lambda,\kappa}$ is a member of the $Z^{\lambda,\kappa}$ set. Thus, the set $Z^{\lambda,\kappa}$ has six members, and the member number J from the set $Z^{\lambda,\kappa}$ with $J = 1, 2, \ldots, 6$ is represented as$Z_j^{\lambda,\kappa}$. Labels for each grid point, their coordinates in the reference configuration, and tags for their neighboring grid points are obtained from an external file.

In the time marching method, t donates the current time and $\Delta t > 0$ presents the time step and $\tau = t + \Delta t$. The Euler method is used to temporally integrate the grain growth equations.

The algorithm used for the time integration method is as follows:

Start the loop on all points of finite element integration points $\lambda = 1, \lambda_{el}$.

- Given macroscale quantities: $\overline{\mathbf{F}}^{\lambda}(t), \overline{\mathbf{T}}^{\lambda}(\tau), \overline{\theta}^{\lambda}(t), \overline{\theta}^{\lambda}(\tau), \overline{\mathbf{T}}^{\lambda}(t)$, H.
- Macroscale quantities to be updated: $\left\{\overline{\mathbf{T}}^{\lambda}(\tau)\right\}$.

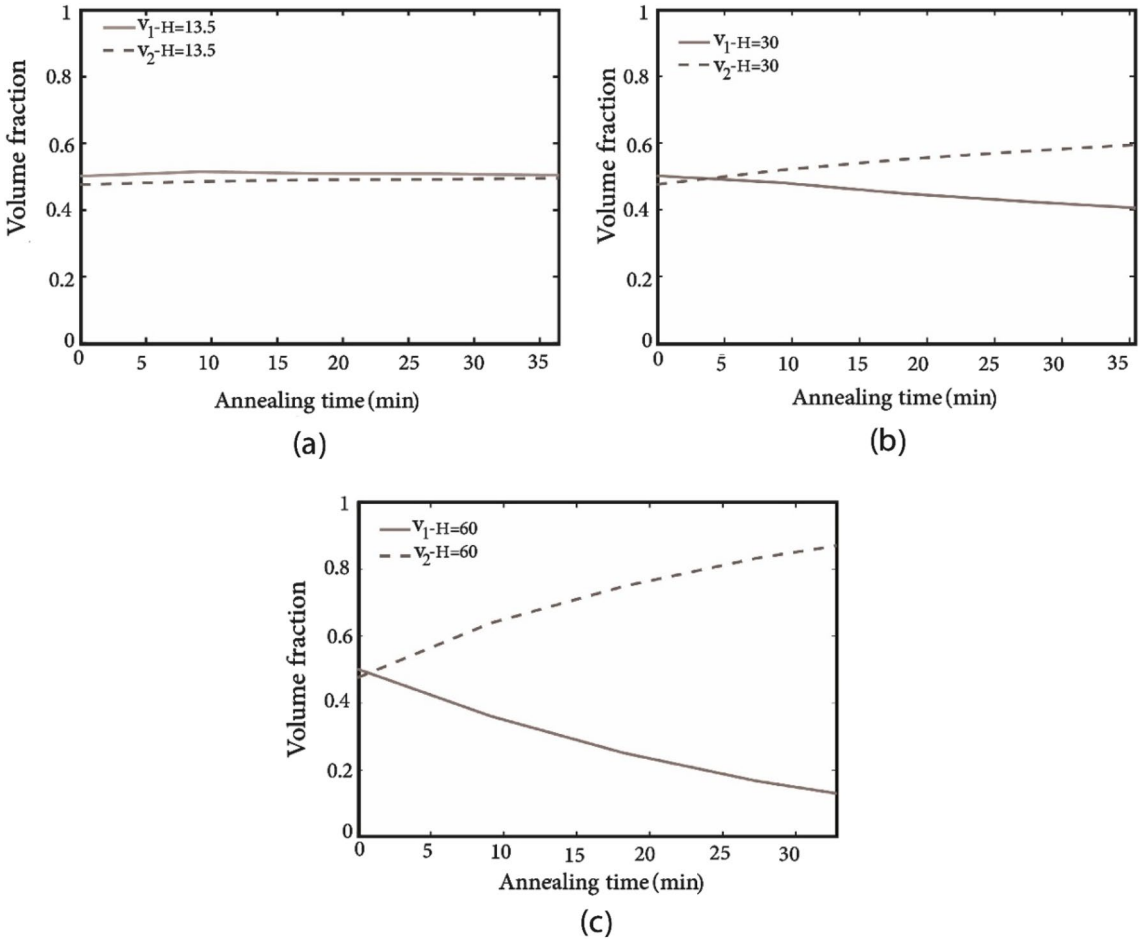

Fig. 10 The simulation results for the VF evolution of grain sets $(0,\ 35,\ \varphi_2)$ and $(180,\ 35,\ \varphi_2)$ for constant strain $\varepsilon = 0.002$ and magnetic field with strengths of **a** $H = 13.5\ \mathrm{MAm^{-1}}$, **b** $H = 30\ \mathrm{MAm^{-1}}$, and **c** $H = 60\ \mathrm{MAm^{-1}}$ over the annealing time

Start the loop on all points of the grid of $k = 1, \Omega$.

- Given mesoscale quantities: $\left\{ \xi_i^{\lambda,k}(t), A_p^{\lambda,k}(t), Z^{\lambda,\kappa} \right\}$.
- Mesoscale quantities to be updated: $\left\{ \xi_i^{\lambda,k}(\tau), A_p^{\lambda,k}(\tau) \right\}$.

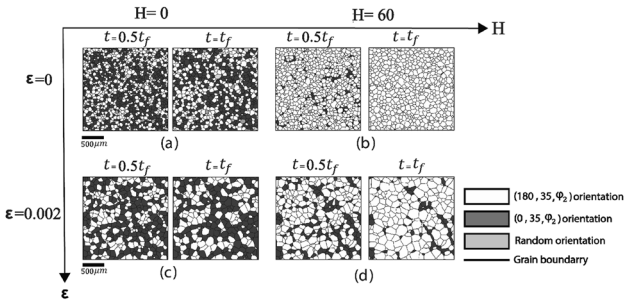

Fig. 11 The simulation results of microstructure evolution for titanium polycrystalline for different strains $\varepsilon = 0,\ 0.002$ and magnetic field with strengths of $H = 0,\ 60\ \mathrm{MAm^{-1}}$ at times $t = 0.5t_\mathrm{f}$ and $t = t_\mathrm{f}$.

Step 1: Determining the deformation gradient tensor at the mesoscale $\mathbf{F}(t)$ and $\mathbf{F}(\tau)$:

$$\mathbf{F}(t) = \overline{\mathbf{F}}^{\lambda}(t) \quad \text{and} \quad \mathbf{F}(\tau) = \overline{\mathbf{F}}^{\lambda}(\tau).$$

Step 2: Specifying the temperature on the mesoscale $\theta(t)$ and $\theta(\tau)$

$$\theta(t) = \overline{\theta}^{\lambda}(t) \quad \text{and} \quad \theta(\tau) = \overline{\theta}^{\lambda}(\tau).$$

Step 3: Calculating the strain tensor at the mesoscale $\mathbf{E}_i(t)$ and $\mathbf{E}_i(\tau)$ for each $i\epsilon A_{\xi}$ species:

$$\mathbf{E}_i(t) = \frac{1}{2\left\{ \left(\mathbf{F}_i(t)\right)^T \mathbf{F}_i(t) - \mathbf{I} \right\}},$$

$$\mathbf{E}_i(\tau) = \frac{1}{2\left\{ \left(\mathbf{F}_i(\tau)\right)^T \mathbf{F}_i(\tau) - \mathbf{I} \right\}}.$$

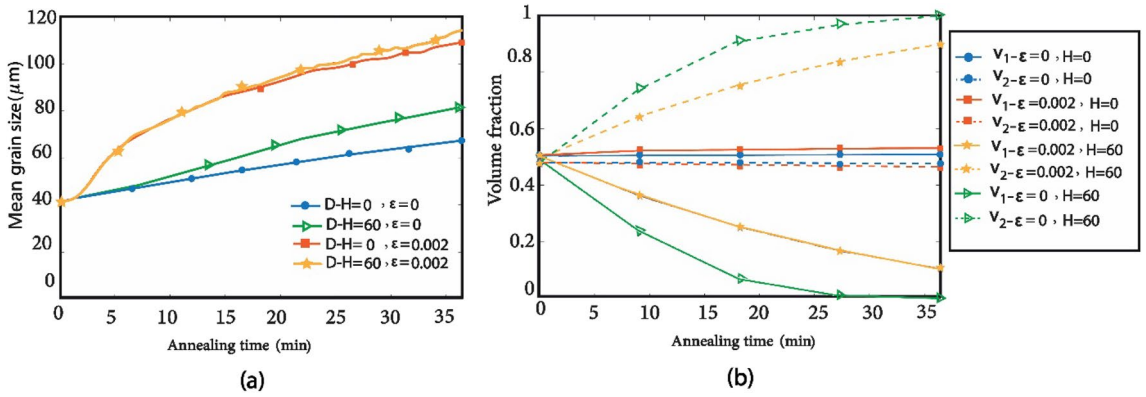

Fig. 12 **a** the mean grain size evolution for all grains; **b** the VF evolution of $(0,\ 35,\ \varphi_2)$ grains and $(180,\ 35,\ \varphi_2)$ grains for different strains $\varepsilon=0$, 0.002, and applied magnetic field with strengths of $H=0$, 60 MAm^{-1} over the annealing time

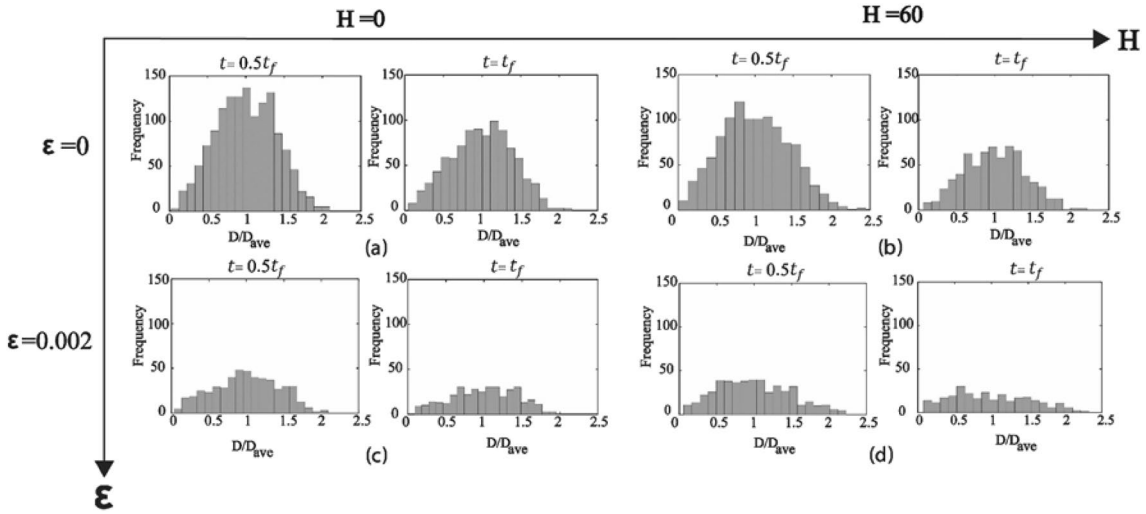

Fig. 13 The simulation results of GSD for different strains $\varepsilon=0$, 0.002, and magnetic field with strengths of $H=0$, 60 MAm^{-1} over the annealing time

Step 4: Determining the set A_ξ of species, which are present at the grid point and its immediate neighbors:

$$A_\xi = \left[\cup_{j=1}^{6} A_p^{\lambda,Z_j^{\lambda,k}}(t)\right] \cup A_p^{\lambda,k}(t).$$

$A_\xi = 1$ indicates no inter-species exchange or transfer and therefore step 11 should be performed after updating the set $A_p^{\lambda,k}(\tau) = A_p^{\lambda,k}(t)$ in $\xi_i^{\lambda,k}(\tau) = \xi_i^{\lambda,k}(t)$ for all $i \in A_p^{\lambda,k}(t)$ species.

Step 5: Calculating the free energies $\psi_i^e(t)$, $\psi_i^M(t)$, $\psi_i^\theta(t)$ on the mesoscale for each $i\epsilon A_\xi$ species:

$$\psi_i^e = {}^1\!/_2\overline{\mathbf{E}}_i : \mathrm{c}_i\left[\overline{\mathbf{E}}_i\right],$$

$$\psi_i^M(t) = \frac{1}{2}\mu_0 H^2 X_i,$$

$$\psi_i^\theta(t) = c_i\left[\left(\theta(t)-\theta_0\right) - \theta(t)\ln(\theta(t)/\theta_0\right].$$

Step 6: Calculating the driving forces for $f_i^\xi(t)$ inter-species exchange for each $i\epsilon A_\xi$ species:

$$f_i^\xi(t) = f_i^m(t) + f_i^e(t) + f_i^\theta(t) + f_i^M(t),$$

$$f_i^m(t) = -\sum_{s\in A_\xi} \frac{\epsilon_{is}^\xi}{2}\nabla^2\xi_i^{\lambda,k}(t) - \sum_{s\in A_\xi} \omega_{is}^\xi \xi_s^{\lambda,k}(t) \quad \text{with} \quad s \neq i,$$

$$f_i^e(t) = \frac{g'\left(\xi_i^{\lambda,k}(t)\right)\left[\sum_{s\in A_\xi} g\left(\xi_s^{\lambda,k}(t)\right)\left(\psi_s^e(t) - \psi_i^e(t)\right)\right]}{\left[\sum_{s\in A_\xi} g\left(\xi_s^{\lambda,k}(t)\right)\right]^2},$$

$$f_i^\theta(t) = \frac{g'\left(\xi_i^{\lambda,k}(t)\right)\left[\sum_{s\in A_\xi} g\left(\xi_s^{\lambda,k}(t)\right)\left(\psi_s^\theta(t) - \psi_i^\theta(t)\right)\right]}{\left[\sum_{s\in A_\xi} g\left(\xi_s^{\lambda,k}(t)\right)\right]^2},$$

$$f_i^M(t) = \frac{g'\left(\xi_i^{\lambda,k}(t)\right)\left[\sum_{s\in A_\xi} g\left(\xi_s^{\lambda,k}(t)\right)\left(\psi_s^M(t) - \psi_i^M(t)\right)\right]}{\left[\sum_{s\in A_\xi} g\left(\xi_s^{\lambda,k}(t)\right)\right]^2}.$$

It is worth noting that $\xi_s^{\lambda,k}(t) = 0$ if $i \notin A_p^{\lambda,k}(t)$. The finite difference method is used to calculate the second-order gradient of the MPF variables $\nabla^2\xi_s^{\lambda,\kappa}(t)$ [44].

$$\nabla^2\xi_s^{\lambda,\kappa}(t) = \frac{\left[\sum_{j=1}^{6} \xi_s^{\lambda,z_j^{\lambda,\kappa}}(t)\right] - 6\xi_s^{\lambda,\kappa}(t)}{z^2}.$$

Step 7a: Calculating the total driving force for the inter-species exchange ($f_{pq}(t)$) for the species $p, q \in A_\xi$ with $p<q$:

$$f_{pq}(t) = f_p^\xi(t) - f_q^\xi(t).$$

Step 7b: Calculating the inter-species transfer rate $\Delta\xi_{pq}$ for $p, q \in A_\xi$ species with $p<q$:

If $\left|f_{pq}(t)\right| > f_{pq}^{\xi,c}$, then, we have:

$$\Delta\xi_{pq} = L_{pq}^\xi(t) f_{pq}(t)\Delta t.$$

where the coefficients of mobility $\widehat{\boldsymbol{L}}_{\boldsymbol{pq}}^{\boldsymbol{\xi}}(\boldsymbol{\theta}(\boldsymbol{t})) = \boldsymbol{L}_{\boldsymbol{pq}}^{\boldsymbol{\xi}}(\boldsymbol{t})$.

If $\left|\boldsymbol{f}_{\boldsymbol{pq}}(\boldsymbol{t})\right| < \boldsymbol{f}_{\boldsymbol{pq}}^{\boldsymbol{\xi},\boldsymbol{c}}$, then, we have:

$$\Delta\xi_{pq} = 0.$$

The set A_ξ contains the quantities $\Delta\xi_{pq} \neq 0$ for the species $p, q \in A_\xi$ with $p<$q. If $A_\xi = \varnothing$, then $\xi_i^{\lambda,k}(\tau) = \xi_i^{\lambda,k}(t)$ for each species is $i\epsilon A_p^{\lambda,k}(t)$; then, the set $A_p^{\lambda,k}(\tau) = A_p^{\lambda,k}(t)$ is updated and then we proceed with step 11.

Step 8: Updating the VF of the species ($\xi_i^{\lambda,k}(\tau)$) for each species $i \in A_\xi$:

$$\xi_i^{\lambda,k}(\tau) = \xi_i^{\lambda,k}(t) + \sum_{p<q} K_{ipq}\Delta\xi_{pq}, \quad p, q \in A_\xi.$$

If $\xi_i^{\lambda,k}(\tau) > 1$, then $\xi_i^{\lambda,k}(\tau) = 1$ and if $\xi_i^{\lambda,k}(\tau) < 0$, then $\xi_i^{\lambda,k}(\tau) = 0$.

Step 9: Updating the set $A_p^{\lambda,k}(\tau)$ of the species, which satisfy the following conditions:

$$0 < \xi_i^{\lambda,k}(\tau) \leq 1, \quad i \in A_\xi.$$

Step 10: Ensuring that the constraint $\sum_{i\epsilon A_p^{\lambda,k}(\tau)} \xi_i^{\lambda,k}(\tau) = 1$ is always satisfied by substituting:

$$\xi_i^{\lambda,k}(\tau) \quad \text{with} \quad \frac{\xi_i^{\lambda,k}(\tau)}{\sum_{s\in A_p^{\lambda,k}(\tau)} \xi_s^{\lambda,k}(\tau)}, \quad i \in A_p^{\lambda,k}(\tau).$$

Step 11: Updating Cauchy stress at mesoscale, $\mathrm{T}^{\lambda,k}(\tau)$:

$$\mathbf{T}^{\lambda,\mathrm{k}}(\tau) = (\det\mathbf{F}(\tau))^{-1}\mathbf{F}(\tau)\mathbf{T}^*(\tau)(\mathbf{F}(\tau))^{\mathrm{T}}.$$

where $\mathrm{T}^*(\tau)$ is the second Piola- Kirchhoff stress on the mesoscale:

$$\mathbf{T}^*(\tau) = \frac{\sum_{i\in A_p^{\lambda,k}(\tau)} g\left(\xi_i^{\lambda,\kappa}(\tau)\right)\left\{C_i\left[\mathbf{E}(\tau) - \lambda_i\left(\theta(\tau) - \theta_0\right)\mathbf{I}\right]\right\}}{\sum_{i\in A_p^{\lambda,k}(\tau)} g\left(\xi_i^{\lambda,\kappa}(\tau)\right)}.$$

The end of the loop is on all grid points of the RVE.

Step A: Updating Cauchy stress at macro scale using Eq. 19:

$$\overline{\mathbf{T}}^{\lambda}(\tau) = \frac{1}{\Omega}\sum_{\kappa=1}^{\Omega} \mathbf{T}^{\lambda,k}(\tau)$$

Step B: Determining the Jacobin matrix for the finite-element code Abaqus/Standard for Newton–Raphson iterations [2, 44].

The end of the loop is on finite element integration points.

Data availability Upon reasonable request, the corresponding author will provide the datasets that support the findings of the current study.

Declarations

Conflict of interest The authors declared no conflicts of interest.

References

1. M. Jamshidian, P. Thamburaja, T. Rabczuk, A multiscale coupled finite-element and phase-field framework to modeling stressed grain growth in polycrystalline thin films. J. Comput. Phys. **327**, 779–798 (2016). https://doi.org/10.1016/j.jcp.2016.09.061
2. P. Thamburaja, M. Jamshidian, A multiscale Taylor model-based constitutive theory describing grain growth in polycrystalline cubic metals. J. Mech. Phys. Solids **63**(1), 1–28 (2014). https://doi.org/10.1016/j.jmps.2013.10.009
3. P. Sonnweber-Ribic, P. Gruber, G. Dehm, E. Arzt, Texture transition in Cu thin films: Electron backscatter diffraction vs. X-ray

diffraction. Acta Mater. **54**(15), 3863–3870 (2006). https://doi.org/10.1016/j.actamat.2006.03.057
4. M. Jamshidian, T. Rabczuk, *Phase field modelling of stressed grain growth: analytical study and the effect of microstructural length scale*, vol. 261 (Academic Press Inc., Cambridge, 2014), pp.23–35
5. T.G. Nieh, J. Wadsworth, Hall-petch relation in nanocrystalline solids. Scr. Metall. Mater. **25**(4), 955–958 (1991). https://doi.org/10.1016/0956-716X(91)90256-Z
6. P.E. Goins, H.A. Murdoch, E. Hernández-Rivera, M.A. Tschopp, Effect of magnetic fields on microstructure evolution. Comput. Mater. Sci. **150**(April), 464–474 (2018). https://doi.org/10.1016/j.commatsci.2018.04.034
7. H. Saito, A. Iwabuchi, T. Shimizu, Effects of Co content and WC grain size on wear of WC cemented carbide. Wear **261**(2), 126–132 (2006). https://doi.org/10.1016/j.wear.2005.09.034
8. K.D. Ralston, N. Birbilis, Effect of grain size on corrosion: a review. Corrosion **66**(7), 0750051–07500513 (2010). https://doi.org/10.5006/1.3462912
9. G. Ben Hamu, D. Eliezer, L. Wagner, The relation between severe plastic deformation microstructure and corrosion behavior of AZ31 magnesium alloy. J. Alloys Compd. **468**(1–2), 222–229 (2009). https://doi.org/10.1016/j.jallcom.2008.01.084
10. C.V. Thompson, R. Carel, Stress and grain growth in thin films. J. Mech. Phys. Solids **44**(5), 657–673 (1996). https://doi.org/10.1016/0022-5096(96)00022-1
11. E. Shahnooshi, M. Jamshidian, M. Jafari, S. Ziaei-Rad, T. Rabczuk, Phase field modeling of stressed grain growth: effect of inclination and misorientation dependence of grain boundary energy. J. Cryst. Growth **518**(February), 18–29 (2019). https://doi.org/10.1016/j.jcrysgro.2019.04.015
12. M. Jafari, M. Jamshidian, S. Ziaei-Rad, D. Raabe, F. Roters, Constitutive modeling of strain induced grain boundary migration via coupling crystal plasticity and phase-field methods. Int. J. Plast. **99**, 19–42 (2017). https://doi.org/10.1016/j.ijplas.2017.08.004
13. M.S. Ghaffari Rad, M. Jafari Gelooyak, M. Jamshidian, A. Saeed, M. Silani, T. Rabczuk, Phase field modelling of normal and stressed grain growth: the effect of RVE size and microscopic boundary conditions. Int. J. Multiscale Comput. Eng. **19**(1), 1–15 (2021). https://doi.org/10.1615/intjmultcompeng.2021035463
14. M. Jafari, M. Jamshidian, S. Ziaei-Rad, B.J. Lee, *Modeling length scale effects on strain induced grain boundary migration via bridging phase field and crystal plasticity methods*, vol. 174–175 (Elsevier Ltd, Amsterdam, 2019)
15. A.D. Sheikh-Ali, D.A. Molodov, H. Garmestani, Migration and reorientation of grain boundaries in Zn bicrystals during annealing in a high magnetic field. Scr. Mater. **48**(5), 483–488 (2003). https://doi.org/10.1016/S1359-6462(02)00508-0
16. A.D. Sheikh-Ali, D.A. Molodov, H. Garmestani, Boundary migration in Zn bicrystal induced by a high magnetic field. Appl. Phys. Lett. **82**(18), 3005–3007 (2003). https://doi.org/10.1063/1.1572536
17. W. Mullins, Magnetically induced grain-boundary motion in bismuth. Acta Metall. **4**(4), 421–432 (1956). https://doi.org/10.1016/0001-6160(56)90033-5
18. D.A. Molodov, P.J. Konijnenberg, Grain boundary dynamics and selective grain growth in non-ferromagnetic metals in high magnetic fields. Zeitschrift fuer Met. Res. Adv. Tech. **96**(10), 1158–1165 (2005). https://doi.org/10.3139/146.101156
19. D.A. Molodov, C. Bollmann, P.J. Konijnenberg, L.A. Barrales-Mora, V. Mohles, Annealing texture and microstructure evolution in titanium during grain growth in an external magnetic field. Mater. Trans. **48**(11), 2800–2808 (2007). https://doi.org/10.2320/matertrans.MI200701
20. D.A. Molodov, N. Bozzolo, Observations on the effect of a magnetic field on the annealing texture and microstructure evolution in zirconium. Acta Mater. **58**(10), 3568–3581 (2010). https://doi.org/10.1016/j.actamat.2010.02.027
21. D.A. Molodov, A.D. Sheikh-Ali, Effect of magnetic field on texture evolution in titanium. Acta Mater. **52**(14), 4377–4383 (2004). https://doi.org/10.1016/j.actamat.2004.06.004
22. D.A. Molodov, C. Günster, G. Gottstein, Grain boundary motion and grain growth in zinc in a high magnetic field. J. Mater. Sci. **49**(11), 3875–3884 (2014). https://doi.org/10.1007/s10853-013-7699-5
23. L.A. Barrales-Mora, V. Mohles, P.J. Konijnenberg, D.A. Molodov, A novel implementation for the simulation of 2-D grain growth with consideration to external energetic fields. Comput. Mater. Sci. **39**(1), 160–165 (2007). https://doi.org/10.1016/j.commatsci.2006.01.026
24. H.C. Lei, X.B. Zhu, Y.P. Sun, L. Hu, W.H. Song, Effects of magnetic field on grain growth of non-ferromagnetic metals: a monte carlo simulation. EPL **85**(3), 38004 (2009). https://doi.org/10.1209/0295-5075/85/38004
25. J.B. Allen, Simulations of anisotropic texture evolution on paramagnetic and diamagnetic materials subject to a magnetic field using Q-state monte carlo. J. Eng. Mater. Technol. Trans. ASME **138**(4), 1–9 (2016). https://doi.org/10.1115/1.4033908
26. T. He, Y. Wang, W. Sun, X. Zhao, The evolution of recrystallized texture of cold-rolled pure copper annealed with a magnetic field in the transverse direction. IOP Conf. Ser. Mater. Sci. Eng. **82**(1), 012055 (2015). https://doi.org/10.1088/1757-899X/82/1/012055
27. P. Sonnweber-Ribic, P.A. Gruber, G. Dehm, H.P. Strunk, E. Arzt, Kinetics and driving forces of abnormal grain growth in thin Cu films. Acta Mater. **60**(5), 2397–2406 (2012). https://doi.org/10.1016/j.actamat.2011.12.030
28. Y. Rezaei, M. Jafari, M. Jamshidian, Phase-field modeling of magnetic field-induced grain growth in polycrystalline metals. Comput. Mater. Sci. **200**, 110786 (2021). https://doi.org/10.1016/J.COMMATSCI.2021.110786
29. J.M. Zhang, K.W. Xu, V. Ji, Strain-energy-driven abnormal grain growth in copper films on silicon substrates. J. Cryst. Growth **226**(1), 168–174 (2001). https://doi.org/10.1016/S0022-0248(01)01376-8
30. S. Bigl, C.O.W. Trost, S. Wurster, M.J. Cordill, D. Kiener, Film thickness dependent microstructural changes of thick copper metallizations upon thermal fatigue. J. Mater. Res. (2017). https://doi.org/10.1557/jmr.2017.199
31. O. Glushko, M.J. Cordill, The driving force governing room temperature grain coarsening in thin gold films. Scr. Mater. **130**, 42–45 (2017). https://doi.org/10.1016/J.SCRIPTAMAT.2016.11.012
32. N. Moelans, B. Blanpain, P. Wollants, An introduction to phase-field modeling of microstructure evolution. Calphad Comput. Coupling Phase Diagrams Thermochem. **32**(2), 268–294 (2008). https://doi.org/10.1016/j.calphad.2007.11.003
33. I. Steinbach, F. Pezzolla, A generalized field method for multiphase transformations using interface fields. Phys. D Nonlinear Phenom. **134**(4), 385–393 (1999). https://doi.org/10.1016/S0167-2789(99)00129-3
34. I. Steinbach, Phase-field models in materials science. Model. Simul. Mater. Sci. Eng. **17**(7), 073001 (2009). https://doi.org/10.1088/0965-0393/17/7/073001
35. S.G. Kim et al., Computer simulations of two-dimensional and three-dimensional ideal grain growth. Phys. Rev. E (2006). https://doi.org/10.1103/PhysRevE.74.061605
36. G. Abrivard, E.P. Busso, S. Forest, B. Appolaire, Phase field modelling of grain boundary motion driven by curvature and stored energy gradients. Part I: theory and numerical implementation. Phil. Mag. **92**(28–30), 3618–3642 (2012). https://doi.org/10.1080/14786435.2012.713135
37. L. Chen et al., An integrated fast Fourier transform-based phase-field and crystal plasticity approach to model recrystallization of three dimensional polycrystals. Comput. Methods Appl. Mech.

Eng. **285**, 829–848 (2015). https://doi.org/10.1016/j.cma.2014.12.007
38. L. Zhao, P. Chakraborty, M.R. Tonks, I. Szlufarska, On the plastic driving force of grain boundary migration: a fully coupled phase field and crystal plasticity model. Comput. Mater. Sci. **128**, 320–330 (2017). https://doi.org/10.1016/j.commatsci.2016.11.044
39. A.M. Roy, Influence of interfacial stress on microstructural evolution in NiAl alloys. JETP Lett. **112**(3), 173–179 (2020). https://doi.org/10.1134/S0021364020150023
40. A.M. Roy, Formation and stability of nanosized, undercooled propagating intermediate melt during $\beta \rightarrow \delta$ phase transformation in HMX nanocrystal. Europhysics Lett. **133**(5), 56001 (2021). https://doi.org/10.1209/0295-5075/133/56001
41. E. Fried, M.E. Gurtin, Dynamic solid-solid transitions with phase characterized by an order parameter. Phys. D Nonlinear Phenom. **72**(4), 287–308 (1994). https://doi.org/10.1016/0167-2789(94)90234-8
42. M. Tonks, P. Millett, Phase field simulations of elastic deformation-driven grain growth in 2D copper polycrystals. Mater. Sci. Eng. A **528**(12), 4086–4091 (2011). https://doi.org/10.1016/j.msea.2011.02.007
43. M. Ledbetter, H. Ogi, S. Kai, S. Kim, M. Hirao, Elastic constants of body-centered-cubic titanium monocrystals. J. Appl. Phys. **95**(9), 4642–4644 (2004). https://doi.org/10.1063/1.1688445
44. M. Jamshidian, G. Zi, T. Rabczuk, Phase field modeling of ideal grain growth in a distorted microstructure. Comput. Mater. Sci. **95**, 663–671 (2014). https://doi.org/10.1016/j.commatsci.2014.08.024